On concomitant gradients in low-field MRI

P.L. Volegov, J.C. Mosher, M.A. Espy, R.H. Kraus Jr. *

Los Alamos National Laboratory, Biological and Quantum Physics Group, Los Alamos, NM 87545, USA

Abstract

Growing interest in magnetic resonance imaging (MRI) at ultra-low magnetic fields (ULF, $\sim\mu$T fields) has been motivated by several advantages over its counterparts at higher magnetic fields. These include narrow line widths, the possibility of novel imaging schemes, reduced imaging artifacts from susceptibility variations within a sample, and reduced system cost and complexity. In addition, ULF NMR/MRI with superconducting quantum interference devices is compatible with simultaneous measurements of biomagnetic signals, a capability conventional systems cannot offer. Acquisition of MRI at ULF must, however, account for concomitant gradients that would otherwise result in severe image distortions. In this paper, we introduce the general theoretical framework that describes concomitant gradients, explain why such gradients are more problematic at low field, and present possible approaches to correct for these unavoidable gradients in the context of a non-slice-selective MRI protocol.

1. Introduction

Conventional approaches to magnetic resonance imaging (MRI) have generally pushed systems to ever higher magnetic field strengths [1]. Higher magnetic fields (commonly 3–10 T or more) are sought to improve signal-to-noise by increasing sample polarization and Larmor frequencies (ω_L, which results in higher signal amplitude in Faraday induction receiver coils). Higher imaging fields also increase resolution since as the signal amplitude increases, smaller voxels will generate the same signal-to-noise. More recently, we have seen increasing interest and progress in ultra-low field (ULF, $\sim\mu$T fields) NMR and MRI. ULF MRI has been motivated by a variety of potential benefits such as smaller magnetic field induced artifacts, narrow NMR linewidths, simultaneous detection of multiple nuclei, and the prospect of systems with reduced cost and size [2].

Such systems could be portable and the sample need not be restricted to the interior of a magnet bore (ex situ or "inside out" imaging). Low-field methods even enable imaging using the earth's magnetic field, $\sim$50 μT [3–8]. Other motivators include the desire to avoid complications associated with high-field MRI of samples and subjects containing metal (i.e., metal pins or implants), that would be essentially eliminated at low fields. Not only can samples containing metal be imaged at ULF, but we recently demonstrated that samples entirely contained within metallic containers can be imaged at ULF [9].

Magnetic resonance imaging at ULF also offers other advantages. Measurement fields (the fields about which the nuclei of interest precess) need not be extremely homogeneous to achieve narrow NMR linewidths. The NMR linewidth scales linearly with the measurement field strength for a fixed relative homogeneity allowing the possibility of very narrow NMR lines with high signal-to-noise at ULF [10]. Narrow NMR linewidth enables high-resolution imaging with minimal field

* Corresponding author. Fax: +1 505 665 4507.
    E-mail address: rkraus@lanl.gov (R.H. Kraus Jr.).

gradients. Susceptibility artifacts, caused by coupling between the applied magnetic field and varying susceptibility within the sample, broaden resonance lines at high fields but are negligible at ULF. The absence of such artifacts should provide opportunities for novel forms of static and functional imaging at ULF such as the possibility of manipulating T1 contrast to provide significant contrast not always realized at high fields [11]. All of these effects combine to offer the prospect that MRI at low fields may provide a regime of high sensitivity and resolution, with unique applications.

NMR and MRI detect the magnetic signature of nuclear spins precessing in the measurement magnetic field at the characteristic Larmor frequency, ω_L. The difficulty of detecting NMR/MRI signals at ULF is primarily due to the decreased spin polarization. Conventional systems using Faraday detection would suffer further reduction of signal amplitude because the induced voltage scales linearly with ω_L, which is proportional to the measurement field. The superconducting quantum interference device (SQUID) is a magnetic flux-to-voltage converter of exquisite sensitivity with a response that is independent of frequency. Consequently, a growing number of low-field NMR/MRI systems have employed SQUID sensors at measurement fields below 10 mT, (e.g., [9,10,12–21]). The frequency-independent response of SQUID detectors readily enables one to simultaneously detect the signatures from multiple nuclei, even when their NMR frequencies may differ by factors of two or more [22].

Finally, demonstrating ULF MRI enables the possibility of acquiring tomographic images simultaneously with sub-millisecond temporal resolution biomagnetic measurements such as magnetoencephalography (MEG) [23]. Acquiring biomagnetic and anatomical data simultaneously will largely eliminate most of the sources of error in co-localizing these data which are currently acquired on separate instruments (such as MEG and conventional anatomical MRI). The co-localization error is commonly an order of magnitude greater than the instrumental resolution of MRI or state-of-the-art MEG [24]. This advance will revolutionize functional brain source localization accuracy for both MEG and EEG.

Various investigators, including ourselves, have already demonstrated that ULF MRI is possible (see for example, [8,18,20,21]). We also demonstrated the feasibility of magnetic resonance measurements with simultaneous magnetoencephalography (MEG), using the same detectors [23], and simultaneous NMR and magnetocardiography (MCG) and magnetomyography (MMG) [22]. These measurements constitute scientific advances necessary to derive bioelectric source localization and anatomical MRI from simultaneously acquired data.

A significant problem encountered at ULF is potentially large distortions caused by *concomitant* gradients,

that is gradients in the directions transverse to the desired (longitudinal) gradient. MRI has traditionally depended on generating linear magnetic field gradients [25] across the sample that cause all of the nuclei within a given planar volume to precess at the same ω_L. Thus, by acquiring signal within a specific frequency window, one naturally selects signal originating only from nuclei within a planar region of the sample commonly referred to as a 'slice.' Maxwell's equations predict that any coil system generating gradients dB_z/dx, dB_z/dy, or dB_z/dz will always generate gradients of transverse components: dB_x/dx, dB_x/dy, etc., that have the same field strength as B_z gradients. If we denote the uniform measurement field at the origin as B_0, the magnitude of the longitudinal ("useful") gradient as $G_\parallel$ and magnitude of the transverse ("concomitant") gradients as $G_\perp$, then we may approximate the frequency variation (spatial encoding) as:

$$\Delta v = \frac{\gamma}{2\pi}\left(\sqrt{(B_0 + G_\parallel)^2 + G_\perp^2} - B_0\right). \tag{1}$$

In typical MRI applications, the desirable frequency encoding is a result of the longitudinal component of applied gradients. We can approximate the frequency variation as:

$$\Delta v \approx \left(\frac{\gamma}{2\pi}G_\parallel\right) + \left(\frac{\gamma}{2\pi}\frac{1}{2}\frac{1}{B_0 + G_\parallel}G_\perp^2\right) = \Delta v_\parallel + \Delta v_\perp. \tag{2}$$

For MR imaging in high fields ($B_0 \approx 1$ T), typical values of these gradients are $dB/dz \approx 2 \times 10^{-2}$ T/m, and a region of interest (ROI) of size $D \approx 0.5$ m. For such a typical case, $G_\parallel/B_0 \ll 1$, $G_\perp/B_0 \ll 1$, $\Delta v_\perp/\Delta v_\parallel < 0.01$, and we see that $\Delta v \approx (\gamma/2\pi)G_\parallel$, i.e., the frequency variation is proportional only to the longitudinal gradients, the common assumption in high-field MRI.

For an ultra-low field MRI scanner, assuming operating parameters of: $B_0 \approx 10^{-4}$ T, $dB/dz \approx 10^{-4}$ T/m, and a smaller volume $D \approx 0.2$ m, we see the range of Larmor frequencies for the longitudinal gradient would be $\Delta v_\parallel \approx 851$ Hz and the impact of concomitant gradients would result in $\Delta v_\perp \approx 84$ Hz. In this example, the frequency shift resulting from the concomitant gradients reaches 10% of total frequency shift due to the primary gradient, even for a small ROI. Concomitant gradients in ULF MRI will clearly result in significant distortions of the frequency and phase encoding relative to the simple planar model of gradients. These gradients will result in correspondingly large displacement and distortion artifacts that must be accounted for in any ULF MRI approach.

Previous studies of concomitant gradient effects and corrections [26], assumed the direction of the measurement field is unperturbed by the gradient, focusing instead on the effect that the amplitude change has on encoding phase. In this paper, we examine the impact that "deflection" of the magnetic field has on the

precession. While previous methods to correct for the concomitant phase use parabolic approximations [27], we present a more accurate reconstruction method and compare it to the previous techniques. Our work will be presented in the context of an example of non-slice selective gradient echo MRI protocol. While we have chosen a specific example to illustrate the quantitative effects of concomitant gradients, our approach can be applied to other sequences and protocols.

In the following sections, we first present the basic theory and the common assumptions for both high- and low-field cases, then demonstrate the significant distortions that occur uniquely at low fields. We present examples of the point spread function (PSF) for both high and low fields, then show novel improvements for more accurately calculating the PSF which is used to correct the concomitant gradient distortions.

2. Theory

2.1. Concomitant gradients

We begin by considering a system of coils that generate the fields and gradients in the volume of interest, such as those shown in Figs. 1 and 2. These and other similar systems widely used in MRI produce fields and gradients that are axi-symmetric with an origin placed in the plane of symmetry. Since the volume is source free, the Maxwell's equations must hold:

$$\nabla \times \mathbf{B}(\mathbf{r}) = 0 \text{ and } \nabla \cdot \mathbf{B}(\mathbf{r}) = 0. \tag{3}$$

In the case of ideal linear gradients, i.e., $\nabla B_z(\mathbf{r}) = \mathbf{g}$, a cylindrical geometry [28], and assuming initial condition $\mathbf{B}(0) = B_0 \hat{\mathbf{e}}_z$, we can express the magnetic field as:

$$\mathbf{B}(\mathbf{r}) = B_0 \hat{\mathbf{e}}_z + \mathbf{G} \cdot \mathbf{r}. \tag{4}$$

The gradient matrix is:

$$\mathbf{G} = \begin{bmatrix} -g_z/2 & 0 & g_x \\ 0 & -g_z/2 & g_y \\ g_x & g_y & g_z \end{bmatrix}, \tag{5}$$

or separating the desirable longitudinal gradient $\mathbf{g}$ from the concomitant gradients yields the equivalent form:

$$\mathbf{B}(\mathbf{r}) = (B_0 + (\mathbf{g} \cdot \mathbf{r}))\hat{\mathbf{e}}_z + \mathbf{G_c}\mathbf{r}, \tag{6}$$

where

$$\mathbf{g} = \begin{bmatrix} g_x \\ g_y \\ g_z \end{bmatrix}, \quad \mathbf{G}_c = \begin{bmatrix} -g_z/2 & 0 & g_x \\ 0 & -g_z/2 & g_y \\ 0 & 0 & 0 \end{bmatrix}. \tag{7}$$

The resulting instantaneous Larmor frequency for spins in the volume is given by

$$\omega(\mathbf{r}, \mathbf{g}) = -\gamma \sqrt{(B_0 + (\mathbf{g} \cdot \mathbf{r}))^2 + \|\mathbf{G_c}\mathbf{r}\|^2}, \tag{8}$$

and if $|B_0| \gg |(\mathbf{g}\,\mathbf{r})|$, then $\omega(\mathbf{r}, \mathbf{g}) \cong -\gamma (B_0 + (\mathbf{g} \cdot \mathbf{r}))$.

These results can be illustrated for typical gradient coil designs. Linear variation in field along the direction of the field (longitudinal gradient dB_z/dz) is readily produced by a simple Maxwell coil (Fig. 1). Linear variation in the direction orthogonal to the field (transverse gradient $dB_z/d\rho$) is best generated by a somewhat more complex saddle-coil, such as the Golay coil (Fig. 2).

2.2. Effects of the concomitant gradients in the gradient echo technique

The gradient echo pulse sequence is a common pulse sequence used in modern high-field MRI. The specific pulse sequence we will use to illustrate concomitant gradient effects consists of an initial RF pulse to tilt the spin population in the region of interest (ROI), followed by pulses G_x and G_y to provide the phase-encoding gradients in the presence of a frequency encoding gradient,
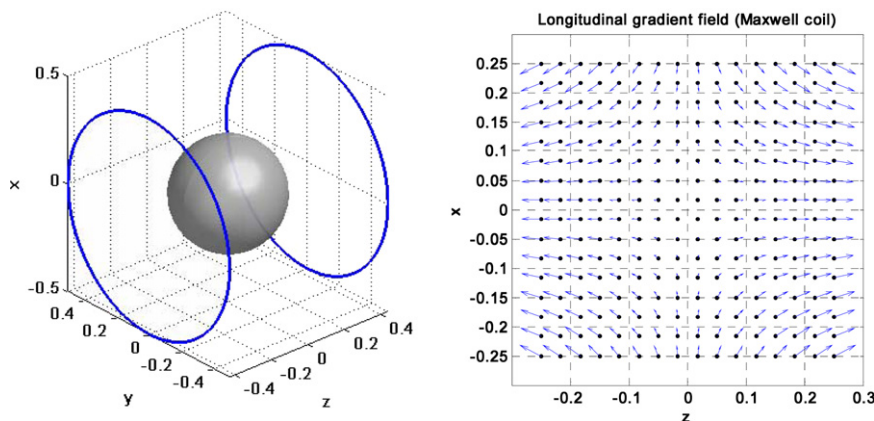

Fig. 1. Diagram of a Maxwell coil and the longitudinal gradient field produced by such a coil set. The field varies linearly (gradient) along the direction of the primary field (longitudinal gradient dB_z/dz).
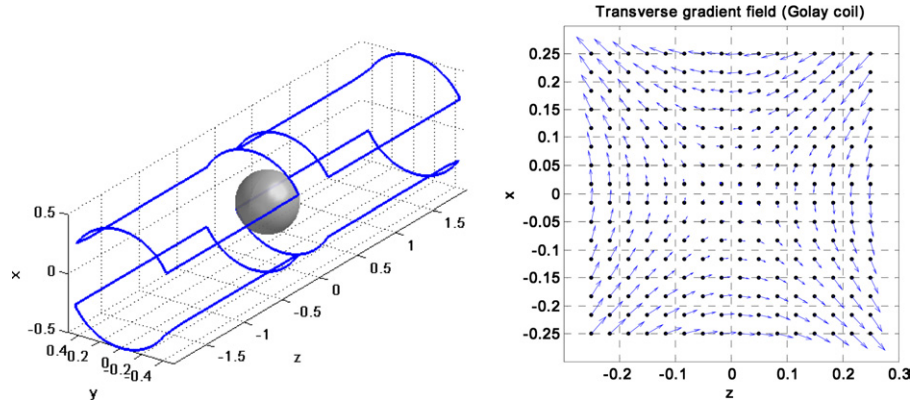
Fig. 2. Diagram of a Golay coil and the transverse gradient field produced by such a coil set. The field varies linearly (gradient) along the direction orthogonal to the field (transverse gradient $dB_z/d\rho$).

G_z The phase encoding gradients are applied in a large number of discrete values (typically 256 up to 512) to sample the applicable k-space. At time t_{ph}, G_x, and G_y are turned off and the sign of G_z is reversed, causing the phases in each voxel to refocus at time $2 \times t_{ph}$, resulting in the echo signal. The gradient G_z also provides frequency encoding in the Z-dimension. The image is reconstructed by 3D inverse Fourier transform. We will use a traditional gradient echo sequence, illustrated in Fig. 3, as a basis for discussing the effect of concomitant gradients on MRI image quality. The exact manifestation of the distortions caused by the concomitant gradients will depend upon the actual technique employed. While we choose a traditional gradient echo technique to illustrate the impact of concomitant gradients on image quality and the effectiveness of various approaches to correcting the distortions, the theoretical framework and approaches to correcting the distortions presented here are completely general.

We assume that a magnetization field $\mathbf{m}(\mathbf{r}, t)$ is present in the volume at time $t = 0$ and that a measurement field $\mathbf{B}(\mathbf{r})$ has been applied to the volume. The conventional assumption at this point is to assume that the gradients have no effect on the field orientation, i.e., $\mathbf{B}(\mathbf{r}) \cong B_0 \hat{\mathbf{e}}_z$, simplifying the solution of the Bloch equation. Here, we retain the "deflection" of the field caused by the gradients to analyze its impact on the measured

signal. To analyze effects of the concomitant gradients we will neglect relaxation times. For a given magnetization $\mathbf{m}(\mathbf{r}, t)$ and an applied magnetic field $\mathbf{B}(\mathbf{r}, t)$, the Bloch equation [29] is:

$$\frac{d}{dt}\mathbf{m}(\mathbf{r}, t) = \gamma([\mathbf{m}(\mathbf{r}, t) \times \mathbf{B}(\mathbf{r}, t)]), \tag{9}$$

where γ is the gyromagnetic ratio. If the orientation of $\mathbf{B}(\mathbf{r}, t)$ does not change with time, then we can write $\mathbf{B}(\mathbf{r}, t) = B(\mathbf{r}, t)\hat{\mathbf{e}}(\mathbf{r})$, i.e., the amplitude of the magnetic field may change, but not the orientation $\hat{\mathbf{e}}(\mathbf{r})$. The Bloch equation can then be written:

$$\frac{d}{dt}\mathbf{m}(\mathbf{r}, t) = -\gamma B(\mathbf{r}, t)[\hat{\mathbf{e}}(\mathbf{r}) \times \mathbf{m}(\mathbf{r}, t)]$$
$$= \omega(\mathbf{r}, t)(\mathbf{A}(\mathbf{r}) \cdot \mathbf{m}(\mathbf{r}, t)), \tag{10}$$

where $\omega(\mathbf{r}, t) \equiv -\gamma B(\mathbf{r}, t)$ is the Larmor frequency, and $\mathbf{A}(\mathbf{r})$ is the matrix representation of the cross product, given by:

$$\mathbf{A}(\mathbf{r}) = \begin{bmatrix} 0 & -e_z(\mathbf{r}) & e_y(\mathbf{r}) \\ e_z(\mathbf{r}) & 0 & -e_x(\mathbf{r}) \\ -e_y(\mathbf{r}) & e_x(\mathbf{r}) & 0 \end{bmatrix}, \tag{11}$$

where the orientation of $\hat{\mathbf{e}}(\mathbf{r})$ depends on the total applied magnetic field. We note that this treatment is valid for the acquisition of a single line of data because the gradient strength does not change with time during the
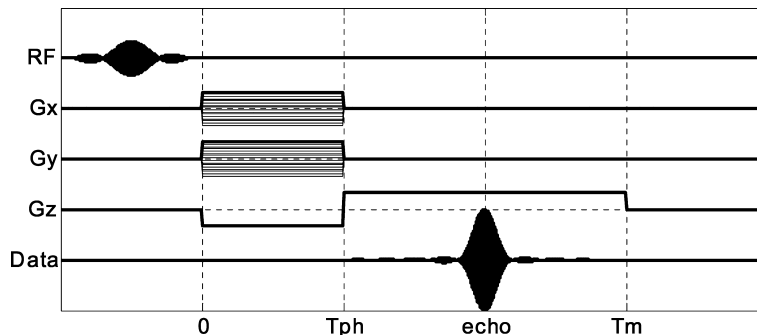

Fig. 3. A typical 3D gradient echo sequence used as a reference to illustrate computed concomitant gradient effects for a general application.

phase encoding or the measurement steps. The eigenvectors of the matrix $\mathbf{A}$ may be expressed as:

$$\mathbf{v}_l : \mathbf{A} \cdot \mathbf{v}_l = \lambda_l \mathbf{v}_l; \quad l = -1, 0, 1;$$
$$\{\lambda_l\}_{-1}^1 \equiv \{-i, 0, i\}; \quad i = \sqrt{-1}, \tag{12}$$

where we note that $\mathbf{v}_{-1} = \mathbf{v}_1^*$, $\mathbf{v}_0 = \hat{\mathbf{e}}(\mathbf{r})$, and the set of eigenvectors form an orthonormal basis. The rotation of the magnetization vector, using $\mathbf{m}_0(\mathbf{r}) \equiv \mathbf{m}(\mathbf{r}, t = 0)$, is then described as:

$$\mathbf{m}(\mathbf{r}, t) = \sum_{l=-1}^1 e^{il \int_0^t \omega(\mathbf{r}, t') \, dt'} \mathbf{v}_l (\mathbf{v}_l^* \cdot \mathbf{m}_0(\mathbf{r})). \tag{13}$$

Finally, the MRI signal one would measure can be expressed as

$$S(t) = \int_V \rho(\mathbf{r}')(\mathbf{p}^* \cdot \mathbf{m}(\mathbf{r}', t)) \, d^3 r', \tag{14}$$

where $\mathbf{p} \equiv \mathbf{p}(\mathbf{r}) \equiv (p_x, p_y, p_z)$ is the sensitivity model of the receiver or sensor, and $\rho(\mathbf{r})$ is spin (nuclear) density. Substituting Eq. (13) into Eq. (14), our rotation model yields:

$$S(t) = \sum_{l=-1}^1 \int_V \rho(\mathbf{r}')(\mathbf{p}^* \cdot \mathbf{v}_l)(\mathbf{v}_l^* \cdot \mathbf{m}_0) e^{il \int_0^t \omega(\mathbf{r}', t') \, dt'} \, d^3 r', \tag{15}$$

where $(\mathbf{p}^* \cdot \mathbf{v}_l)(\mathbf{v}_l^* \cdot \mathbf{m}_0)$ is total spatial sensitivity of the system. If we further assume that the measurement field remains constant, then the Larmor frequency is constant, yielding $\int_0^t \omega(\mathbf{r}, t') \, dt' = \omega(\mathbf{r})t$. Thus, the magnetization vector at time t may be expressed as $\mathbf{m}(\mathbf{r}, t) = \sum_{l=-1}^1 e^{il\omega(\mathbf{r})t} \mathbf{v}_l(\mathbf{v}_l^* \cdot \mathbf{m}_0(\mathbf{r}))$.

Let us now consider the specific gradient echo pulse sequence as outlined in Fig. 3. The gradient echo technique consists of two steps: (1) phase encoding between time 0 and t_{ph}, and (2) measurement from t_{ph} to t_m. The magnetic field is described by Eq. (6). Assuming the gradients (and the total field) are held constant during each step, the resulting MRI signal can be written as:

$$S(t) = \sum_{l=1}^1 \sum_{l'=-1}^1 \int_V \rho(\mathbf{r}')(\mathbf{p}^* \cdot \mathbf{u}_l)(\mathbf{u}_l^* \cdot \mathbf{v}_{l'})(\mathbf{v}_{l'}^* \cdot \mathbf{m}_0)$$
$$\times e^{il\omega_m t} e^{il'\omega_{ph} t_{ph}} \, d^3 r', \tag{16}$$

where $\{\mathbf{v}_l \equiv \mathbf{v}_l(\mathbf{r}, \mathbf{g}_{ph})\}_{-1}^1$ and $\{\mathbf{u}_l \equiv \mathbf{u}_l(\mathbf{r}, \mathbf{g}_m)\}_{-1}^1$ are eigenvectors of the matrix $\mathbf{A}$ determined for the gradients $\mathbf{g}_{ph}$ and $\mathbf{g}_m$ applied during phase encoding and measurement portions of the pulse sequence, respectively. This measurement is repeated for multiple phase encoding and measurement fields $\mathbf{B}(\mathbf{r}) = (B_0 + (\mathbf{g} \cdot \mathbf{r}))\hat{\mathbf{e}}_z + \mathbf{G_c} \cdot \mathbf{r}$, as depicted graphically in Fig. 3, where the concomitant gradients are completely specified by the longitudinal gradients, $\mathbf{g}$. Similarly, $\omega_{ph} \equiv \omega_{ph}(\mathbf{r}, \mathbf{g}_{ph})$ and $\omega_m \equiv \omega_m(\mathbf{r}, \mathbf{g}_m)$ are the Larmor frequencies of spins

in the volume of interest during phase encoding and measurement, respectively.

The Larmor frequencies of spins can be written as:

$$\omega(\mathbf{r}, \mathbf{g}) = -(\gamma B_0 + \gamma(\mathbf{g} \cdot \mathbf{r}) + \Delta\omega(\mathbf{r}, \mathbf{g})), \tag{17}$$

where, $\Delta\omega(\mathbf{r}, g)$ is the additional frequency shift that occurs due to the concomitant gradients,

$$\Delta\omega(r, g) = -\gamma\left(\sqrt{(B_0 + \mathbf{g} \cdot \mathbf{r})^2 + |\mathbf{G}_c\mathbf{r}|^2} - (B_0 + \mathbf{g} \cdot \mathbf{r})\right). \tag{18}$$

Using quadrature phase sensitive detection, the complex MRI signal $\widetilde{S}(t, \mathbf{g}_{ph}, \mathbf{g}_m)$, defined as $\widetilde{S}(t, \mathbf{g}_{ph}, \mathbf{g}_m) \equiv lowpass\{S(t, \mathbf{g}_{ph}, \mathbf{g}_m)e^{-i\omega_0 t}\}$, where $\omega_0 = -\gamma B_0$, can be written using Eq. (16) as:

$$\widetilde{S}(t, \mathbf{g}_{ph}, \mathbf{g}_m) = \sum_{l=-1}^1 e^{il\omega_0 t_{ph}} \int_V \rho(\mathbf{r}')(\mathbf{p}^* \cdot \mathbf{u}_{+1})(\mathbf{u}_{+1}^* \cdot \mathbf{v}_l)$$
$$\times (\mathbf{v}_l^* \cdot \mathbf{m}_0)e^{-i \cdot (\gamma(\mathbf{g}_m \cdot \mathbf{r}') + \Delta\omega_m)t}$$
$$\times e^{-il(\gamma(\mathbf{g}_{ph} \cdot \mathbf{r}') + \Delta\omega_{ph})t_{ph}} \, d^3 r', \tag{19}$$

where only terms with $\mathbf{u}_{+1}$ survive the lowpass filter and $\mathbf{g}_{ph}$ and $\Delta\omega_{ph}$ are the gradient and frequency shift due to concomitant gradients during phase encoding step, respectively; and $\mathbf{g}_m$ and $\Delta\omega_m$ are the gradient and frequency shifts due to concomitant gradients during measurement, respectively. We now transform $\widetilde{S}$ from $(t, \mathbf{g}_{ph}, \mathbf{g}_m)$ coordinate space into k-space using $\mathbf{k} = \gamma(\mathbf{g}_m t + \mathbf{g}_{ph} t_{ph})$ and $\mathbf{k}_{ph} = \gamma \mathbf{g}_{ph} t_{ph}$, giving:

$$\widetilde{S}(\mathbf{k}) = \sum_{l=-1}^1 e^{ili\omega_0 t_{ph}} \int_V \rho(\mathbf{r}')(\mathbf{p}^* \cdot \mathbf{u}_{+1})(\mathbf{u}_{+1}^* \cdot \mathbf{v}_l)(\mathbf{v}_l^* \cdot \mathbf{m}_0)$$
$$\times e^{-i(\mathbf{k} \cdot \mathbf{r}')}e^{-i(l-1)(\mathbf{k}_{ph} \cdot \mathbf{r}')}e^{-i(\varphi_m + l\varphi_{ph})} \, d^3 r', \tag{20}$$

where the phase shifts $\varphi_m \equiv \varphi_m(\mathbf{r}, \mathbf{k}) = \Delta\omega_m t$ and $\varphi_{ph} \equiv \varphi_{ph}(\mathbf{r}, \mathbf{k}) = \Delta\omega_{ph} t_{ph}$ are due to concomitant gradients applied during the phase encoding and measurement portions of the sequence, respectively. φ_{ph} results from concomitant gradients of all applied gradients, while φ_m results from concomitant gradients of g_z (see Fig. 3).

The reconstructed image may be found using an inverse Fourier transform, $\tilde{\rho}(\mathbf{r}) = \int_K e^{i\mathbf{k} \cdot \mathbf{r}} \widetilde{S}(\mathbf{k}) \, d^3 k$, giving:

$$\tilde{\rho}(\mathbf{r}) = \int_V \rho(\mathbf{r}') \sum_{l=-1}^1 e^{il\omega_0 t_{ph}} \int_K (\mathbf{p}^* \cdot \mathbf{u}_{+1})(\mathbf{u}_{+1}^* \cdot \mathbf{v}_l)(\mathbf{v}_l^* \cdot \mathbf{m}_0)$$
$$\times e^{-i(\mathbf{k} \cdot (\mathbf{r}' - \mathbf{r}))}e^{-i(l-1)(\mathbf{k}_{ph} \cdot \mathbf{r}')}e^{-i(\varphi_m + l\varphi_{ph})} \, d^3 k \, d^3 r'. \tag{21}$$

That is, the reconstructed image is represented by a linear operator acting on the original spin density distribution described by:

$$\tilde{\rho}(\mathbf{r}) = \int_V \rho(\mathbf{r}')K(\mathbf{r}, \mathbf{r}') \, d^3 r', \tag{22}$$

where the kernel of the operator (or point spread function) is:

$$K(\mathbf{r}, \mathbf{r}') = \sum_{l=-1}^{1} e^{il\omega_0 t_{ph}} \int_K (\mathbf{p}^* \cdot \mathbf{u}_{+1})(\mathbf{u}_{+1}^* \cdot \mathbf{v}_l)(\mathbf{v}_l^* \cdot \mathbf{m}_0)$$
$$\times e^{-i(\mathbf{k}\cdot(\mathbf{r}'-\mathbf{r}))} e^{-i(l-1)(\mathbf{k}_{ph}\cdot\mathbf{r}')} e^{-i(\varphi_m + l\varphi_{ph})} d^3k. \quad (23)$$

During the acquisition of a single line of data, eigenvectors of the infinitesimal rotation matrix $\mathbf{u}_l$ do not explicitly depend on $\mathbf{k}$. Using definition of k-space variables to express t as a function of $\mathbf{k}$ and recollecting that $\mathbf{g}_m \| \hat{\mathbf{e}}_z$, the phase shift due to concomitant gradients during this step equals:

$$\varphi_m = (\mathbf{k} \cdot \Delta\mathbf{r}') + \phi; \quad \Delta\mathbf{r}' \equiv \Delta\mathbf{r}'(\mathbf{r}') = \frac{\Delta\omega_m}{\gamma(\mathbf{g}_m \cdot \hat{\mathbf{e}}_z)} \hat{\mathbf{e}}_z;$$

$$\phi \equiv \phi(\mathbf{r}') = -\Delta\omega_m \frac{(\mathbf{g}_{ph} \cdot \hat{\mathbf{e}}_z)}{(\mathbf{g}_m \cdot \hat{\mathbf{e}}_z)} t_{ph}. \quad (24)$$

Taking this into account, the Eq. (23) can be re-written as:

$$K(\mathbf{r}, \mathbf{r}') = e^{-i\phi} \sum_{l=-1}^{1} e^{il\omega_0 t_{ph}} \int_K Q_l(\mathbf{r}', \mathbf{k}) e^{-i(\mathbf{k}\cdot(\mathbf{r}'+\Delta\mathbf{r}'-\mathbf{r}))}$$
$$\times e^{-i(l-1)(\mathbf{k}_{ph}\cdot\mathbf{r}')} e^{-il\varphi_{ph}} d^3k, \quad (25)$$

where $Q_l(\mathbf{r}', \mathbf{k}) = (\mathbf{p}^* \cdot \mathbf{u}_{+1})(\mathbf{u}_{+1}^* \cdot \mathbf{v}_l)(\mathbf{v}_l^* \cdot \mathbf{m}_0)$. In previously derived descriptions of concomitant gradients, the magnetization deflection is ignored and $Q_l(\mathbf{r}', \mathbf{k}) = (\mathbf{p}^* \cdot \tilde{\mathbf{e}}_{+1})(\tilde{\mathbf{e}}_{+1}^* \cdot \mathbf{m}_0)\delta_{+1,l}$; $\tilde{\mathbf{e}}_0 = \hat{\mathbf{e}}_z$; $\tilde{\mathbf{e}}_{\pm 1} = (\hat{\mathbf{e}}_x \pm i\hat{\mathbf{e}}_y)/\sqrt{2}$ is assumed. To better illustrate the improvements in the PSF derived here over previously described effects of concomitant gradients we write the eigenvector product as:

$$Q_l(\mathbf{r}', \mathbf{k}) = Q_{+1}^0(\mathbf{r}')(\delta_{+1,l} + \varepsilon_l(\mathbf{r}', \mathbf{k})), \quad (26)$$

where $Q_{+1}^0(\mathbf{r}') = (\mathbf{p}^* \cdot \tilde{\mathbf{e}}_{+1})(\tilde{\mathbf{e}}_{+1}^* \cdot \mathbf{m}_0)$ is total spatial sensitivity in the ideal case and $\varepsilon_l(\mathbf{r}', \mathbf{k})$ is the consequence of the magnetic field deflection. At high field, the common assumption is that $\varepsilon_l(\mathbf{r}', \mathbf{k})$ is zero; however, at low field this vector deflection can result in noticeable distortion as we will discuss further below.

We express the point spread function as a sum of 4 components:

$$K(\mathbf{r}, \mathbf{r}') = K_+(\mathbf{r}, \mathbf{r}') + \widetilde{K}_+(\mathbf{r}, \mathbf{r}') + K_-(\mathbf{r}, \mathbf{r}') + K_0(\mathbf{r}, \mathbf{r}'), \quad (27)$$

where:

$$K_+(\mathbf{r}, \mathbf{r}') = Q_{+1}^0(\mathbf{r}') e^{-i(\phi + \omega_0 t_{ph})} \int_K e^{-i(\mathbf{k}\cdot(\mathbf{r}'+\Delta\mathbf{r}'-\mathbf{r}))} e^{-i\varphi_{ph}} d^3k,$$

$$\widetilde{K}_+(\mathbf{r}, \mathbf{r}') = Q_{+1}^0(\mathbf{r}') e^{-i(\phi + \omega_0 t_{ph})}$$
$$\times \int_K \varepsilon_{+1}(\mathbf{r}', \mathbf{k}) e^{-i(\mathbf{k}\cdot(\mathbf{r}'+\Delta\mathbf{r}'-\mathbf{r}))} e^{-i\cdot\varphi_{ph}} d^3k,$$

$$K_-(\mathbf{r}, \mathbf{r}') = Q_{+1}^0(\mathbf{r}') e^{-i(\phi - \omega_0 t_{ph})} \quad (28)$$
$$\times \int_K \varepsilon_{-1}(\mathbf{r}', \mathbf{k}) e^{-i(\mathbf{k}\cdot(\mathbf{r}'+\Delta\mathbf{r}'-\mathbf{r}))} e^{i2(\mathbf{k}_{ph}\cdot\mathbf{r}')} e^{i\varphi_{ph}} d^3k,$$

$$K_0(\mathbf{r}, \mathbf{r}') = Q_{+1}^0(\mathbf{r}') e^{-i\phi}$$
$$\times \int_K \varepsilon_0(\mathbf{r}', \mathbf{k}) e^{-i(\mathbf{k}\cdot(\mathbf{r}'+\Delta\mathbf{r}'-\mathbf{r}))} e^{i(\mathbf{k}_{ph}\cdot\mathbf{r}')} d^3k.$$

The $K_+(\mathbf{r}, \mathbf{r}')$ term is similar to the conventional PSF; however it includes the effect of a more precise expression for the frequency shift $\Delta\omega_m$ that is implicit in the phase, φ_{ph}, and $\Delta\mathbf{r}'$. In addition, while terms $\widetilde{K}_+(\mathbf{r}, \mathbf{r}')$, $K_-(\mathbf{r}, \mathbf{r}')$, and $K_0(\mathbf{r}, \mathbf{r}')$ are assumed to be negligible at high field, they contribute noticeable distortions at low field. We shall describe and illustrate with simulations the manifestation of each of these terms in the following section.

2.3. Simulation and analysis

From Eqs. (25) and (28) it will become evident that the distortion of an image due to concomitant gradients during the measurement step (distortions along frequency encoded dimension) does not introduce blurring of the image and is limited to reversible geometrical $\rho(\mathbf{r}) \Rightarrow \rho(\mathbf{r} + \Delta\mathbf{r})$ and multiplicative $\rho(\mathbf{r}) \Rightarrow f(\mathbf{r})\rho(\mathbf{r})$ distortions. The magnitude of these distortions as a function of the gradient/field ratio is shown in Fig. 4. For our example gradient echo sequence, the displacement
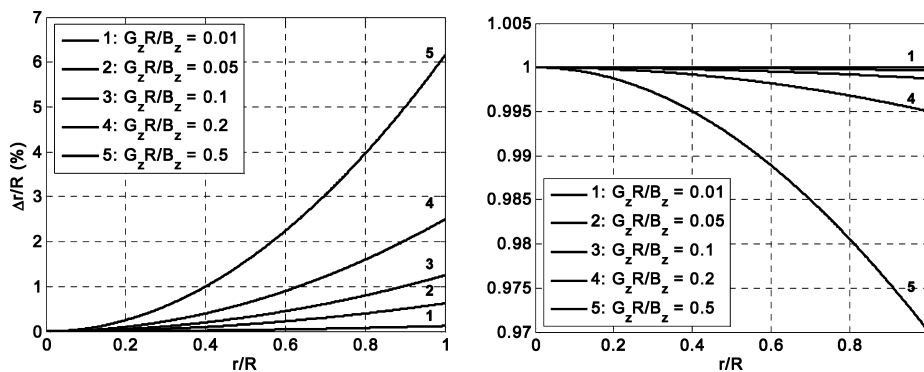

Fig. 4. Geometrical (left) and multiplicative (right) measurement distortions (as defined in the text) due to concomitant gradients shown as a function of relative position within the sample volume (region of interest). Geometrical distortions caused by concomitant gradients approach 7% where the applied gradient field approaches half of the measurement field at the outer extent of the ROI. Multiplicative distortions approach 3% for such a case.
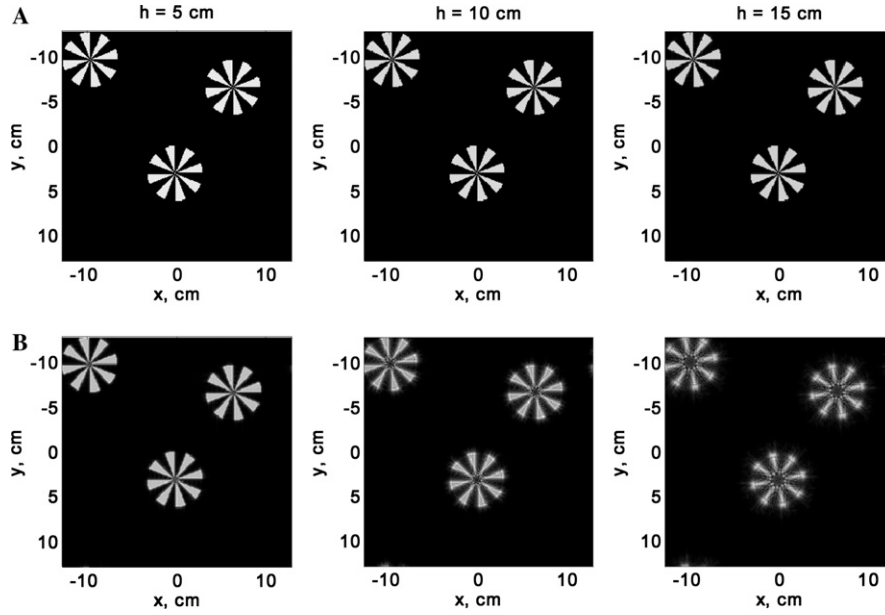
Fig. 5. A comparison of computed distortions due to frequency shift caused by concomitant gradients in the phase encoding step of a gradient echo image for three different distances from the origin along the frequency encoding axis (figure columns). The figure rows represent typical high-field and ULF MRI examples, respectively: (row A) $B_0 = 1$ T, $\max|\mathbf{g}| = 2 \times 10^{-2}$ T/m; (row B) $B_0 = 1 \times 10^{-4}$ T, $\max|\mathbf{g}| = 50 \times 10^{-6}$ T/m.

distortions from the concomitant gradients amount to 7% of the region-of-interest (ROI) while the variation of spatial sensitivity amounts to only 3% of the ROI, even for very large gradient/field ratios. Reconstructing high-quality images must correct for these effects.

Distortions caused during the phase encoding step by the scalar products $(\mathbf{u}_{+1}^+ \cdot \mathbf{v}_l)(\mathbf{v}_l^+ \cdot \mathbf{m}_0)$—the magnetic field deflection—and by the frequency shift due to concomitant gradients, introduce blurring along phase encoding dimensions because these functions depend on $\mathbf{k}$. Fig. 5 clearly illustrates the dramatic difference between distortions caused by concomitant gradients at typical high field compared with ULF MRI. Distortions caused by frequency shift during phase encoding (i.e., due to $e^{-i\varphi_{ph}}$ term) are illustrated in the Fig. 6, where a test image consisting of a uniform grid of spin density delta-functions in the plane of phase encoding dimensions.

While there is no qualitatively obvious distortion for any of the regions of interest (h) at high field, distortions are obvious and severe by $h = 10$ cm for the ULF case. At high fields, there is little need to correct for distortions caused by concomitant gradients, consequently little attention has been paid to this correction beyond first order effects [30]. At ULF, however, concomitant gradients severely distort the images and careful corrections of these effects to high order must be derived and implemented. It can be shown that the distortions due to concomitant gradients during phase encoding step are defined by two dimensionless parameters: $\alpha = \max|\mathbf{g}|h/B_z$ and $\tilde{h} = h/a$, where h is the distance to the symmetry plane of phase encoding gradient coils, and image resolution, a, is defined according to the Nyquist criteria:

$$a = \frac{1}{2(\gamma/2\pi)\max|\mathbf{g}|t_{ph}} \tag{29}$$

and $B_z = B_0 - \max|\mathbf{g}|h$.

To describe the overall characteristic of these distortions, we will use two parameters: (a) the width of the module of point spread function at half height (Δw), and (b) the displacement of the PSF maximum (Δd). For high-field MRI scanners ($B_0 \gg |\mathbf{g}|R$) it is common to retain only lowest order concomitant gradient terms in Eq. (18) to correct for the distortions:

$$\Delta\omega(\mathbf{r}, \mathbf{g}) \approx -\gamma \frac{1}{2} \cdot \frac{\|\mathbf{G}_c \cdot \mathbf{r}\|^2}{B_0}. \tag{30}$$

Using this approximation of the frequency shift due to concomitant gradients, it can be shown[1] that the width of the PSF linearly depends on a product of the parameters α and $\tilde{h}$:

---

[1] Width and displacement of the PSF are estimated using the following integral:

$$\int_{-1/(2\Delta x)}^{1/(2\Delta x)} e^{i2\pi(kx + \alpha^2(k+\beta)^2)} \, dk = \frac{1}{2\alpha} e^{-i2\pi\left(\frac{1}{4}\left(\frac{x}{\alpha}\right)^2 - \alpha^2\beta^2\right)} [C(\xi + x/\alpha + 2\alpha\beta)$$
$$- iS(\xi + x/\alpha + 2\alpha\beta)]_{-\alpha/\Delta x}^{\alpha/\Delta x},$$

where $C(x)$ and $S(x)$ are Fresnel integrals. Fresnel integrals are antisymmetrical functions, so the width of the functions $C(a + x + b) - C(-a + x + b)$ and $S(a + x + b) - S(-a + x + b)$ are symmetrical with respect to $\xi = x + b$, and the width of these functions at half height is equal to $2a$.
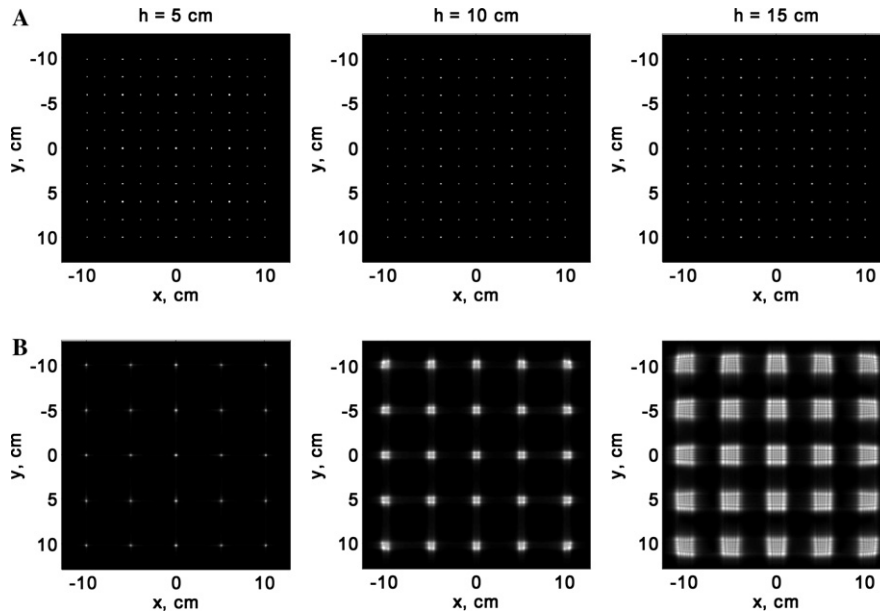
Fig. 6. A comparison of the point spread function due to frequency shift caused by concomitant gradients in the phase encoding step of a gradient echo image for three different distances from the origin along the frequency encoding axis (figure columns). The figure rows represent typical high-field and ULF MRI examples, respectively: (row A) $B_0 = 1$ T, $\max|\mathbf{g}| = 2 \times 10^{-2}$ T/m; (row B) $B_0 = 1 \times 10^{-4}$ T, $\max|\mathbf{g}| = 50 \times 10^{-6}$ T/m.

$$\Delta w = 2\alpha\tilde{h} = \frac{2\max|\mathbf{g}|h^2}{B_z a}. \tag{31}$$

The displacement of the PSF center is:

$$\Delta\mathbf{d} = \frac{\max|\mathbf{g}|h\mathbf{r}}{B_z}, \tag{32}$$

where $\mathbf{r}$ is a displacement from the image center.

As we observed above, while the parabolic approximation (Eq. (30)) is adequate to correct for distortions caused by concomitant gradients at high-field MRI application, it is inadequate for ULF MRI. Significantly, better results can be achieved by expanding Eq. (18) about $|\mathbf{G}_c\mathbf{r}|/B_0 + \mathbf{g}\cdot\mathbf{r}$, keeping the first-order terms, and using:

$$\Delta\omega(\mathbf{r}, \mathbf{g}) \approx -\gamma\frac{1}{2}\cdot\frac{\|\mathbf{G}_c\cdot\mathbf{r}\|^2}{B_0 + \mathbf{g}\cdot\mathbf{r}}. \tag{33}$$

Fig. 7 illustrates ULF MRI computed images for different approximations of the distortions caused by concomitant gradients at two different gradients. Column A are the computed images including an exact representation of the distortions caused by concomitant gradients as presented in Eq. (18). The distortions included in the parabolic approximation (Eq. (30)) is shown in Fig. 7, column B and the more precise approximation derived here (Eq. (33)) is shown in Fig. 7, columns C. The images in Fig. 7 were computed for a ULF MRI measurement field of $B_0 = 1 \times 10^{-4}$ T, and two different gradients and sample sizes: $\max|\mathbf{g}| = 50 \times 10^{-6}$ T/m and

$h = 15$ cm (row 1), and $\max|\mathbf{g}| = 100 \times 10^{-6}$ T/m and $h = 10$ cm. A larger sample size, h, is used for the smaller gradient computation for visualization purposes. It is immediately evident that the parabolic approximation grossly underestimates the actual distortions (illustrated in the exact calculation, Fig. 7, column A) caused by concomitant gradients at ULF, while the more precise approximation of Eq. (33) estimates the distortions quite accurately. Thus, Fig. 7 dramatically demonstrates that a parabolic approximation *will not* be sufficient to correct for concomitant gradient distortions at ULF.

The distortion represented by each term of Eq. (28) is illustrated in Fig. 8. The 'true' image is shown in the upper left frame, the primary image, K_+ is shown in frame 'A,' and the distortions $\widetilde{K}_+(\mathbf{r}, \mathbf{r}')$, $K_-(\mathbf{r}, \mathbf{r}')$, and $K_0(\mathbf{r}, \mathbf{r}')$ are illustrated in frames 'B,' 'C,' and 'D,' respectively. The distortion effect of the $\widetilde{K}_+(\mathbf{r}, \mathbf{r}')$ term represents a slightly increased blurring of the primary image, K_+. The $K_0(\mathbf{r}, \mathbf{r}')$ term describes the effect of concomitant field deflection causing a portion of the deflected polarization vector not to precess about the measurement field, hence that portion of the polarization population is not phase encoded and remains at the origin. The $K_-(\mathbf{r}, \mathbf{r}')$ term represents a "Nyquist ghost" image that appears reflected across the plane of symmetry.

Distortions caused by the deflection of magnetic field away from z-axis during phase encoding and measurement steps are described by the terms $\widetilde{K}_+(\mathbf{r}, \mathbf{r}')$, $K_-(\mathbf{r}, \mathbf{r}')$, and $K_0(\mathbf{r}, \mathbf{r}')$ (Eq. (28)). To quantitatively assess the effect of deflections of the magnetization field, we choose an
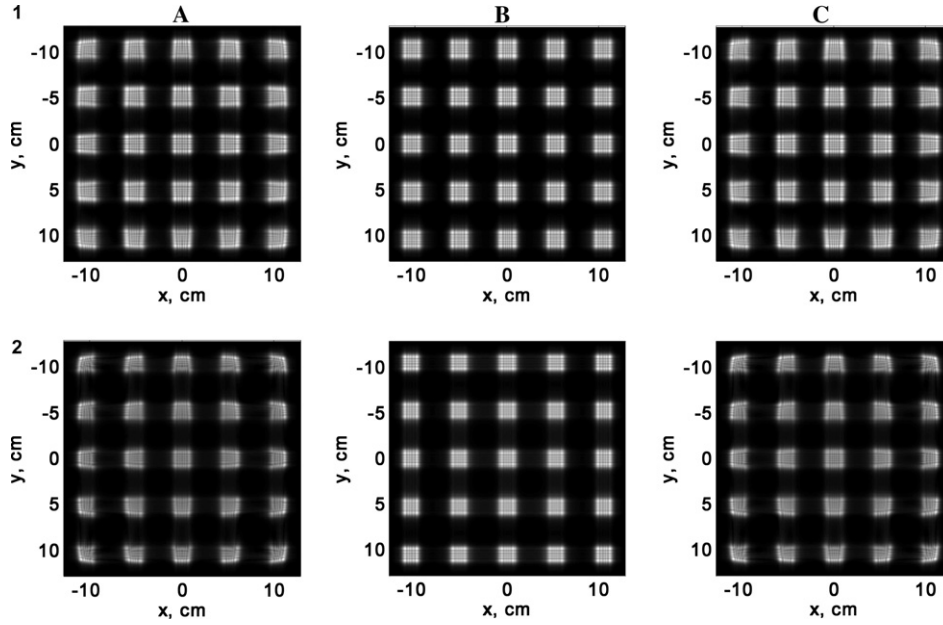
Fig. 7. A comparison of the computed distortions caused by concomitant gradients in gradient echo ULF images ($B_0 = 1 \times 10^{-4}$ T) at two different gradients and for different concomitant gradient approximations. (row 1) $\max|\mathbf{g}| = 50 \times 10^{-6}$ T/m, $h = 15$ cm, (row 2) $\max|\mathbf{g}| = 100 \times 10^{-6}$ T/m, $h = 10$ cm. The columns illustrate the distortions computed using the exact representation of concomitant gradients (column A), the parabolic approximation (column B), and the more precise approximation (defined in the text, column C). It is immediately clear that the distortions computed using a parabolic approximation (column B) do not accurately represent the real distortions (column A) while the approximation we derived (column C) accurately represents them.

initial magnetization $\mathbf{m_0}$, and coil sensitivity $\mathbf{p}$ aligned along x-axis, and using only the lowest order of magnitude terms we have:

$$\varepsilon_{+1}(\mathbf{r},\mathbf{k}) = \frac{\alpha^2}{2}((\tilde{k}_x - \beta x) - \mathrm{i}(\tilde{k}_y - \beta y))^2 + O(\alpha^4),$$

$$\varepsilon_0(\mathbf{r},\mathbf{k}) = 2\alpha^2(\tilde{k}_x - \beta x)((\tilde{k}_x - \beta x) + \mathrm{i}(\tilde{k}_y - \beta y)) + O(\alpha^4),$$

$$\varepsilon_{-1}(\mathbf{r},\mathbf{k}) = \alpha^2\left((\tilde{k}_x - \beta x)^2 + \frac{((\tilde{k}_x - \beta x) + \mathrm{i}(\tilde{k}_y - \beta y))^2}{2}\right) + O(\alpha^4),$$

(34)

where $\tilde{\mathbf{k}} = a\mathbf{k}$, $\beta = g_z/4\max|\mathbf{g}|h$ and we recall $\alpha = \max|\mathbf{g}|h/B_z$. A sense of the magnitude of these distortions can be gained by simulating an ULF MRI image acquired using the following parameters: ($B_0 = 1 \times 10^{-4}$ T, $\max|\mathbf{g}| = 50 \times 10^{-6}$ T/m, $h = 20$ cm). We find the maximum distortion caused by the deflection of the magnetization vector to be 1% for each term in the point spread function ($\widetilde{K}_+(\mathbf{r},\mathbf{r}')$, $K_-(\mathbf{r},\mathbf{r}')$, and $K_0(\mathbf{r},\mathbf{r}')$) relative to the main term $K_+(\mathbf{r},\mathbf{r}')$. Alternatively, one can state that ignoring magnetization deflection caused by concomitant gradients will cause up to 3% of the spin density of the actual object is mislocalized. While this effect is relatively small, the effect grows quadratically with the region of interest size (due to the α^2 term in Eq. (34)). Additionally, more dramatic effects will be seen for objects with high-spin densities near the periphery of the ROI.

3. Discussion and conclusions

The pursuit of MRI at ULF by our group and others has necessitated a re-examination of distortions caused by concomitant gradients. We introduce the general theoretical framework describing concomitant gradients for MRI imaging systems from which we derive a model of the effect of concomitant gradients on image distortion that is more precise than previously published treatises of the subject. While ignoring the magnetization vector deflection and using a simple parabolic approximation for $\Delta\omega(\mathbf{r},g)$ are sufficient to compute high-resolution images from high-field MRI measurements, we have shown that such simple corrections are insufficient to correct for these distortions at low- and ultra low-fields. We presented a model that includes a more precise description of frequency (and resulting phase) distortions than previous parabolic approximations. In addition, we describe the deflection of the magnetization vector caused by concomitant gradients that has heretofore been ignored. Utilizing these more accurate representations of concomitant gradients in computing images from magnetic resonance data is necessary to realize high-resolution MRI at ultra low-magnetic fields.

Acquisition of MRI at ULF must accurately account for concomitant gradient induced effects on both frequency and total magnetization vector that result in severe image distortions. We have presented a detailed analysis of the mathematical description of concomitant
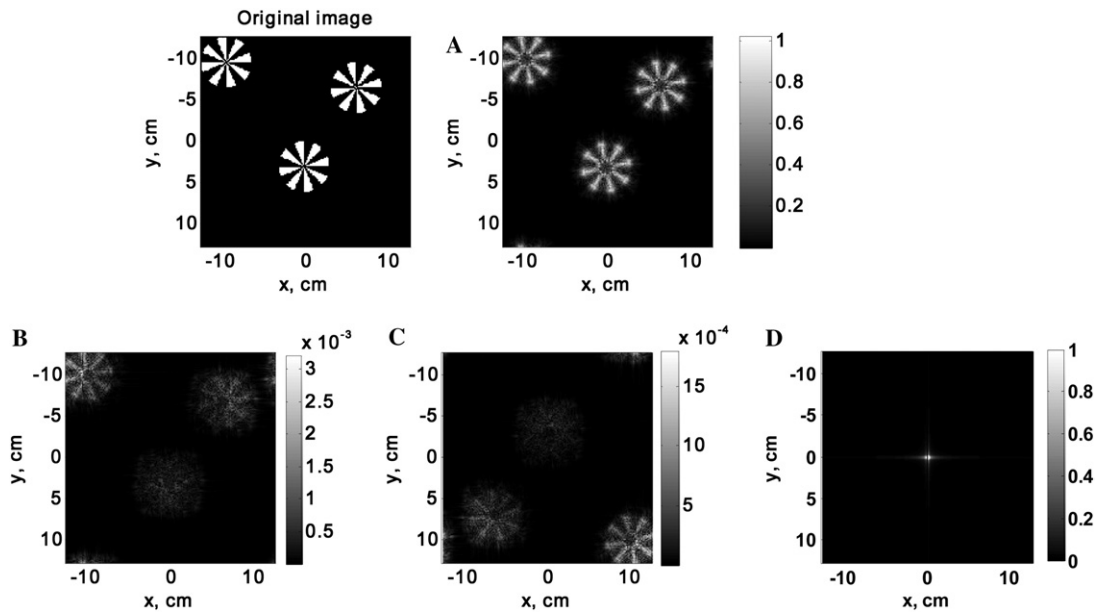
Fig. 8. Illustration of computed distortions represented by each term of Eq. (28) (see text) relative to the 'true' image (top-left panel) assuming ULF imaging parameters of $B_0 = 1 \times 10^{-4}$ T, $\max|\mathbf{g}| = 50 \times 10^{-6}$ T/m. The panels represent only the spin density in the 'true' image that is distorted by concomitant gradients highlighting the importance of accounting for these effects in any inverse applied to ULF data. While the distortions in panel A are commonly corrected (with less accurate description of the $\Delta\omega_{\mathrm{m}}$ in generating MRI images, the distortions illustrated in panels B–D and correction methodology is derived here for the first time.

gradients where the practical effect of each term is illustrated by a computed graphical image distortion. We compared the distortions resulting from the model presented here to previously derived models and to the exact solution. We demonstrated that image distortions *at ULF* are insufficiently approximated by previous models of concomitant gradients and a more precise description, as outlined here, must be used to correct for these effects to realize high-quality images. We observe that in the ideal case, transverse components of the gradients dB_z/dx, dB_z/dy depend only on z, thus the effect of concomitant gradients is revealed in 3D and can be avoided in true 2D objects, by placing the object in $z = 0$ plane and using dB_z/dx, dB_z/dy gradients.

Conventional MRI has pushed the limits of high-field imaging to enhance signal-to-noise and resolution. Low- and ultra-low field MRI measured by SQUID sensors has recently attracted attention because of a broad range of potential benefits including smaller susceptibility artifacts, narrow NMR linewidths, reduced field homogeneity requirements, simultaneous detection of multiple nuclei, and the prospect of systems with reduced cost and size. ULF MRI also enables imaging of samples containing metallic materials and even inside of metallic containers [9].

A significant goal of our work is to integrate ULF MRI with sub-millisecond temporal resolution biomagnetic measurements such as magnetoencephalography (MEG) [23]. Simultaneous acquisition of MEG (and other biomagnetic data) and anatomical data will enable

superposition of functional and anatomical data without the error inherent with current techniques of co-localizing data sets from separate MEG and MRI measurements. This advance could revolutionize functional brain source localization accuracy for both MEG and EEG.

References

[1] X. Hu, D.G. Norris, Advances in high-field magnetic resonance imaging, Annu. Rev. Biomed. Eng. 6 (2004) 157–184.
[2] A. Macovski, S. Conolly, Novel approaches to low cost MRI, Magn. Reson. Med. 30 (1993) 221–230.
[3] J. Stepišnic, V. Eržen, M. Kos, NMR imaging in the Earth's magnetic field, Magn. Reson. Med. 15 (1990) 386–391.
[4] G.J. Bene, Nuclear magnetism of liquid systems in the Earth field range, Physics Reports 58 (1980) 213–267.
[5] G.J. Bene, Spin echoes in zero mean field, Comptes Rendus Hebdomadaires des Seances de l'Academie des Sciences Serie B 271 (1970) 1235–1237.
[6] R.K. Cooper, J.A. Jackson, Remote (inside-out) NMR.I. Remote production of a region of homogeneous magnetic field, J. Magn. Reson. 41 (1980) 400–405.
[7] L.J. Burnett, J.A. Jackson, Remote (inside-out) NMR. II. Sensitivity of NMR detection for external samples, J. Magn. Reson. 41 (1980) 406–410.
[8] J.A. Jackson, L.J. Burnett, J.F. Harmon, Remote (inside-out) NMR. III. Detection of nuclear magnetic resonance in a remotely produced region of homogeneous magnetic field, J. Magn. Reson. 41 (1980) 411–421.
[9] A.N. Matlachov, P.L. Volegov, M.A. Espy, J.S. George, R.H. Kraus Jr., SQUID detected NMR in microtesla magnetic fields, J. Magn. Reson. 170 (2004) 1–7.

[10] R. McDermott, A.H. Trabesinger, M. Mück, E.L. Hahn, A. Pines, J. Clarke, Liquid-state NMR and scalar couplings in microtesla magnetic fields, Science 295 (2002) 2247–2249.

[11] U.A. Ramadan, A.T. Markkola, J. Halavaara, J. Tanitu, A.M. Hakkinen, H.J. Aronen, On- and off resonance spin-lock MT imaging of normal human brain at 0.1 T: possibilities to modify image contrast, Magn. Reson. Imag. 16 (1998) 1191–1199.

[12] N.Q. Fan, M.B. Heaney, J. Clarke, D. Newitt, L.L. Wald, E.L. Hahn, A. Bielecki, A. Pines, Nuclear magnetic resonance with DC SQUID preamplifiers, IEEE Trans. Magn. 25 (1989) 1193–1199.

[13] M.P. Augustine, D.M. TonThat, J. Clarke, SQUID detected NMR and NQR, Solid State Nucl. Magn. Reson. 11 (1998) 139–156.

[14] K. Schlenga, R.F. McDermott, J. Clarke, R.E. de Souza, A. Wong-Foy, A. Pines, Low-field magnetic resonance imaging with a High-Tc dc superconducting quantum interference device, Appl. Phys. Lett. 75 (1999) 3695–3697.

[15] H.C. Seton, D.M. Bussell, J.M.S. Hutchison, I. Nicholson, D.J. Lurie, DC SQUID-based NMR detection from room temperature samples, Phys. Med. Biol. 37 (1992) 2133–2138.

[16] H.C. Seton, J.M.S. Hutchison, D.M. Busell, A 4.2 K receiver coil and SQUID amplifier used to improve SNR of low-field magnetic resonance images of the human arm, Meas. Sci. Technol. 8 (1997) 198–207.

[17] H.C. Seton, J.M.S. Hutchison, D.M. Bussell, A tuned SQUID amplifier for MRI based on a DOIT flux locked loop, IEEE Trans. Appl. Supercond. 7 (1997) 3213–3216.

[18] S. Kumar, B.D. Thorson, W.F. Avrin, Broadband SQUID NMR with room-temperature samples, J. Magn. Reson. B 107 (1995) 252–259.

[19] S. Kumar, W.F. Avrin, B.R. Whitecotton, NMR of room temperature samples with a flux-locked dc SQUID, IEEE Trans. Magn. 32 (1996) 5261–5264.

[20] S. Kumar, R. Mathews, S.G. Haupt, D.K. Lathrop, M. Takigawa, J.R. Rozen, S.L. Brown, R.H. Koch, Nuclear magnetic resonance using a high temperature superconducting quantum interference device, Appl. Phys. Lett. 70 (1997) 1037–1039.

[21] R. McDermott et al., SQUID-detected magnetic resonance imaging in microtesla magnetic fields, J. Low Temp. Phys. 135 (2004) 793–821.

[22] M.A. Espy, A.N. Matlachov, P.L. Volegov, J.C. Mosher, J.S. George, R.H. Kraus Jr., SQUID-based simultaneous detection of NMR and biomagnetic signals at ultra-low magnetic fields, IEEE Trans. Superconductivity, (2005), in press.

[23] P. Volegov, A.N. Matlachov, M.A. Espy, J.S. George, R.H. Kraus Jr., Simultaneous magnetoencephalography and SQUID detected nuclear MR in microtesla magnetic fields, Magn. Reson. Med. 52 (2004) 467–470.

[24] R.H. Kraus Jr., P. Volegov, K. Maharajh, M.A. Espy, A.N. Matlashov, E.R. Flynn, Performance of a novel SQUID-based superconducting imaging-surface magnetoencephalography system, Phys. C 368 (2002) 18–23.

[25] E. Mark Haacke, R.W. Brown, M.R. Thompson, R. Venkatesan, Magnetic Resonance Imaging: Physical Principles and Sequence Design, Wiley, New York, 1999.

[26] D.G. Norris, J.M.S. Hutchison, Concomitant magnetic field gradients and their effects on imaging at low magnetic field strength, Magn. Reson. Imag. 8 (1990) 33–37.

[27] Xiaohong Joe Zhou, Y.P. Du, M.A. Bernstein, H.G. Reynolds, J.K. Maier, J.A. Polzin, Concomitant magnetic-field-induced artifacts in axial echo planar imaging, Magn. Reson. Med. 39 (1998) 596–605.

[28] R.M. Weisskoff, M.S. Cohen, R.R. Rzedzian, Nonaxial whole-body instant imaging, Magn. Reson. Med. 29 (1993) 796–803.

[29] E.T. Jaynes, Matrix treatment of nuclear induction, Phys. Rev. 98 (4) (1955) 1099–1105.

[30] Y.P. Du, X.J. Zhou, M.A. Bernstein, Correction of concomitant magnetic field-induced image artifacts in nonaxial echo-planar imaging, Magn. Reson. Med. 48 (2002) 509–515.